



Using laser marking to engrave optimal patterns for in-plane displacement and strain measurement

Quentin Bouyra, Benoît Blaysat, Hélène Chanal, Michel Grédiac

► To cite this version:

Quentin Bouyra, Benoît Blaysat, Hélène Chanal, Michel Grédiac. Using laser marking to engrave optimal patterns for in-plane displacement and strain measurement. *Strain*, In press, 10.1111/str.12404 . hal-03541996

HAL Id: hal-03541996

<https://hal.science/hal-03541996>

Submitted on 25 Jan 2022

HAL is a multi-disciplinary open access archive for the deposit and dissemination of scientific research documents, whether they are published or not. The documents may come from teaching and research institutions in France or abroad, or from public or private research centers.

L'archive ouverte pluridisciplinaire **HAL**, est destinée au dépôt et à la diffusion de documents scientifiques de niveau recherche, publiés ou non, émanant des établissements d'enseignement et de recherche français ou étrangers, des laboratoires publics ou privés.



Distributed under a Creative Commons Attribution - ShareAlike 4.0 International License

Using laser marking to engrave optimal patterns for in-plane displacement and strain measurement

Q. Bouyra¹, B. Blaysat¹, H. Chanal¹, M. Grédiac^{1†}

¹*Clermont Auvergne Université, CNRS, Clermont Auvergne INP, Institut Pascal, F-63000 Clermont-Ferrand, France*

[†] *corresponding author, michel.grediac@uca.fr*

Abstract: The checkerboard constitutes the best pattern for in-plane displacement and strain measurement because it maximizes image gradient. The use of laser marking to deposit such a pattern on flat surfaces is investigated in this paper. Optimal settings for the parameters influencing the quality of the pattern are given. This pattern being periodic, the images are processed with the Localized Spectrum Analysis, which is one of the spectral techniques used to process such images. It is shown that the metrological performance in terms of measurement resolution is equivalent to the one obtained with transferred checkerboards. Compared to the classic transfer technique generally used to deposit such patterns, the benefit of using laser marking is its ease of use, a much higher print speed and the fact that a thin coat of white paint instead of a thicker layer of white adhesive is employed to ensure a good contrast in the images. Various examples of strain measurements are given, in particular the measurement of the strain field around a knot embedded in a wood specimen subjected to a tensile test.

Keywords: checkerboard, digital image correlation, laser marking, localized spectrum analysis, optimal pattern, wood

1. Introduction

Non-interferometric full-field measurement techniques such as Digital Image Correlation (DIC) are now widespread in the experimental mechanics community. The associated image processing procedures used to retrieve displacement and strain fields from images have been widely studied in many papers and the different parameters influencing the quality of the final result are now well known, which enables experimentalists to employ such measuring tools for material characterization purposes [1]. From a computational point of view, the performance of such systems has globally stabilized and their performance now mainly depends on external parameters such as computer power and digital camera performance. Whatever the image processing procedure used, the sought information is however always encoded in images, so the way this information is encoded also deeply influences the quality of

the final results. Concerning DIC, developing optimal patterns is addressed in various recent papers, see [2, 3, 4, 5, 6, 7, 8, 9, 10] for instance.

A desired pattern being defined, having a printing technique able to reliably reproduce it onto specimens in the best possible way is the crux of the problem. Airbrushing and paint spraying are cheap and popular pattern depositing techniques but it is clear that mastering those techniques to obtain certain global pattern quality criteria such as the mean and the distribution of the size of the dots as well as a uniform spatial distribution is somewhat tricky, if not impossible in practice. Some more sophisticated techniques have been described in the literature. They are of interest when not only global parameters are to be obtained on the printed pattern, but when localized details are to be faithfully reproduced. This is for instance the case for the types of pattern defined in [2, 3, 4]. Ref [11] reports various techniques such as stamping [12], lithography [13], UV photolithography [14], temporary tattoo [15] or the use of TEM (in case of regular grids at microscale [16]) as potential printing techniques in this case. The aim of this paper is to consider another technique, namely laser marking, which seems only having been scarcely used hitherto for this purpose [11, 17], and to delve into its use as a marking device of flat surfaces of specimens.

Concerning the optimal pattern for in-plane displacement and strain measurements, it is worth remembering that the contrast and the image gradient, which can be estimated for instance with the Mean Intensity Gradient (MIG) [18], are the main influencing image parameters driving the quality of measurements performed with DIC, both being expected to be maximized. The contrast being assumed to be optimal, Ref. [3] claims that the checkerboard is theoretically the optimal pattern since the MIG is maximum with this type of pattern geometry. The problem is however that DIC cannot manage such periodic patterns if the displacement is greater than the period of this pattern. Ref. [3, 4] thus propose patterns, which sufficiently depart from the checkerboard so that DIC converges. To stick with this optimal pattern, Ref. [19] proposes to extract displacement fields from checkerboards images by using one of the spectral techniques available to process periodic patterns, see [20] for a complete comparison between these techniques. In addition, it is demonstrated in [21] that under mild

assumptions, minimizing the optical residual in the spatial domain, as DIC does, can advantageously be switched to the frequency domain when periodic patterns are considered. Indeed, in this case, a closed-form solution is available, and this is precisely the formula, which is classically used in all the procedures developed to extract displacement/strain fields from periodic patterns. Employing periodic patterns depends however on the ability to deposit such patterns on the surface of the specimens to be tested. The challenge is that the period is intermediary between large scale, i.e. millimetric periods, which can easily be printed with a printer able to directly print patterns onto flat rigid surfaces, and small-scale (“small” meaning that the period is equal to some micrometers), for which practical solutions are also available, see [22, 23, 24] for instance. Depositing periodic patterns with intermediary values of the period, thus corresponding to some periods per millimeter, can be made by using the technique proposed in [25]. With this technique, the pattern is first printed onto a polymeric sheet by using a high-resolution (up to 50,800 dots per inch) photoplotter. The black pattern is then transferred onto the surface by using a white adhesive. Grids or checkerboards of period as low as $100\ \mu\text{m}$ can be printed with this technique. Another solution is presented in Refs. [26, 27, 28]. It relies on a high resolution printer. It enables the authors to deposit periodic patterns such as grids, but with lower frequencies than the preceding technique since the minimum value is about 3 lines/mm.

In this study, we investigated in depth the settings, which must be used in order to print checkerboards on flat specimens made of various materials such as aluminum, steel, wood and polymer. The idea was first to spray paint the surface of those specimens in white and then to engrave small black squares to form a checkerboard. We considered a challenging case, with a checkerboard of period $p = 100\mu\text{m}$. It means that small squares of size $50\mu\text{m} \times 50\mu\text{m}$ constituted the smallest repetitive square unit. This small quantity enabled us to compare the performance of the patterns obtained with the present engraving system on the one hand, and the one obtained with the classic pattern transfer technique proposed in [25], for which $p = 100\ \mu\text{m}$ is the smallest period which can be obtained.

In this context, the paper is organized as follows. We first start by describing the main features of the laser marker used in this study. The fluctuation of the nominal frequency of the checkerboards

engraved with this device is then studied. The noise level in displacement and strain maps obtained with a checkerboard pattern deposited with laser marking on the one hand, and its counterpart observed with the classic transferring procedure on the other hand, are also compared with a specimen equipped with these two types of checkerboards. The performance of the present engraved pattern technique is finally illustrated with strain maps on a wood specimen in which a knot is embedded.

2. Marker settings

2.1. Principle of laser marking

The laser marker used in this paper is the MDU1000C marker made by Keyence. This printing device is generally used for engraving small QR codes, barcodes, letters or numerals onto flat surfaces, not really for metrology purposes. This marker is equipped with a YVO₄ UV laser featuring a wavelength of 355 nm. This value is about three times lower than the wavelength of standard lasers, which is 1064 nm. Such lasers feature high absorption rate on a variety of materials. The irradiated light is therefore more efficiently absorbed by the surface. In addition, the power does not need to be increased to obtain a highly visible mark [29]. An interesting consequence of using lasers with a low wavelength to mark surfaces is that the heat stress is low, hence the term “cold marking”. It is worth emphasizing that this technique does not involve the use of ink. The basic idea is that the surface of the material at the focal point is changed by the energy delivered by the laser. “Changing” means here vaporization, flaking or fracturation, depending on the nature of the material impacted by the laser. In the present case, we considered flat surfaces spray painted in white, the consequence of a laser hit being that the white color locally turned into black, which induces locally contrasted patterns. According to the datasheet of the supplier, the maximum surface size that can be printed with this marker is $125 \times 125 \text{ mm}^2$. Specimens placed side by side can potentially be printed at the same time as long as they do not cover altogether this maximum area. Stepped, inclined, cylindrical and cone targets can be marked but these possibilities were not tested during this study.

2.2. Influencing parameters

The standard use of the marker consists of loading an image saved for instance in a jpeg file. The controller then behaves like a black box and engraves the corresponding pattern on the surface by adjusting by itself the following influencing parameters:

1. Laser power: the maximum power is equal to 3 W at 40 kHz, but the value at the focal point is 2.5 W only. The laser power can be adjusted between 0 and this maximum value;
2. Spot variable: this setting corresponds to a slight defocus. Defocusing means that the focus plane is shifted along the direction of the beam, thus perpendicularly to the surface to be marked. The amplitude of this shift ranges between -5 mm and +5 mm with respect to the surface. The apparent diameter of the spot increases as this defocus increases or decreases;
3. Repetition: this is the number of passes of the laser, i.e. the number of times the same pattern is printed at the same place. The higher this number, the more marked the contrast of the resulting pattern.
4. Scan speed: this is the movement speed of the laser spot. Its maximum value is 12,000 mm/s. This is quite high but it is worth remembering that no mechanical system is involved, thus no inertia effect may slow down this movement. This speed should ideally be high to ensure a rapid printing of the whole pattern;
5. Pulse frequency: this is the frequency at which a pulse is emitted by the system. The higher this frequency, the lower the spot energy. This quantity lies between 40 and 400 kHz.

However, preliminary tests (not discussed here) show that this procedure does not lead to high-quality printed checkerboards. Indeed, this option is effective for standard printing applications, not really for marking surfaces with tiny details and well mastered shape, color and more importantly, high contrast. We therefore followed a second option which consists of feeding the controller with a dxf file containing the geometrical features of the pattern to be printed as well as the toolpath. All or only some of the five parameters above can then be set by the user in this case, which gives room for defining procedures that are optimal for checkerboard engraving. We first started by adjusting

the first three parameters above, the last two being equal to default values. However, the patterns obtained with this solution were not satisfactory, so we finally had to move on to the direct setting of the whole set of five parameters.

It is finally worth noting that a laser marker basically prints small dots, which can be merged to form more sophisticated forms such as lines. A minimal diameter of 25 μm s is reported by the supplier for these dots. In practice, experiments performed during this study show that this diameter is equal to 32 μm . The question is now to examine how to combine all these parameters to achieve a better quality than that obtained with the standard procedure described above.

2.3. Seeking the best settings

A sensitive issue is that adjusting the parameters must take into account the nature of the material beneath the layer of paint. For instance, if we consider laser power, spot variable and repetition as fixed parameters, and scan speed and pulse frequency as adjustable ones, a simplistic approach consists in thinking that increasing scan speed while decreasing pulse frequency in proportion leads to the same pattern. Preliminary tests show that it is not the case, presumably because some other parameters depending of the material such as the heat diffusion coefficient also influences the results.

Another remark is that the checkerboards to be printed are made of small squares. Since we were interested here in engraving checkerboards made of small squares, it is clear that with circular spots, only shapes approximating such small squares can be obtained, see Figure 1. This point is not really an issue since checkerboard images are obtained by sampling the actual distribution of gray levels. In addition, cameras are equipped with a lens, which is always characterized by a certain Point Spread Function (PSF). This manifests itself by a slight blur of the sharp details such as square borders in checkerboard images. In practice, such “squares” were therefore obtained by following two different routes. The first one consists in printing side by side four small circles with a diameter equal to 32 μm . The centers of these dots were horizontally or vertically shifted from the center of each “square” by a certain quantity equal to $\pm s$. The second one was obtained in plotting first the four preceding spots, and then a fifth one at the center of the square defined by the centers of the four circles. Choosing one

of the two options depends on the nature of the material whose surface must be marked. It has been observed that apart from steel, the second option with five circles of diameter $32\ \mu\text{m}$ and $s = \pm 8\ \mu\text{m}$ is the best one.

The period of the pattern is set by combining scan speed and pulse frequency. In this context, various combinations were investigated for these two latter parameters as well as for the three others listed above which all influence the final result, in addition to the geometric properties of the dot (diameter, distance s between centers).

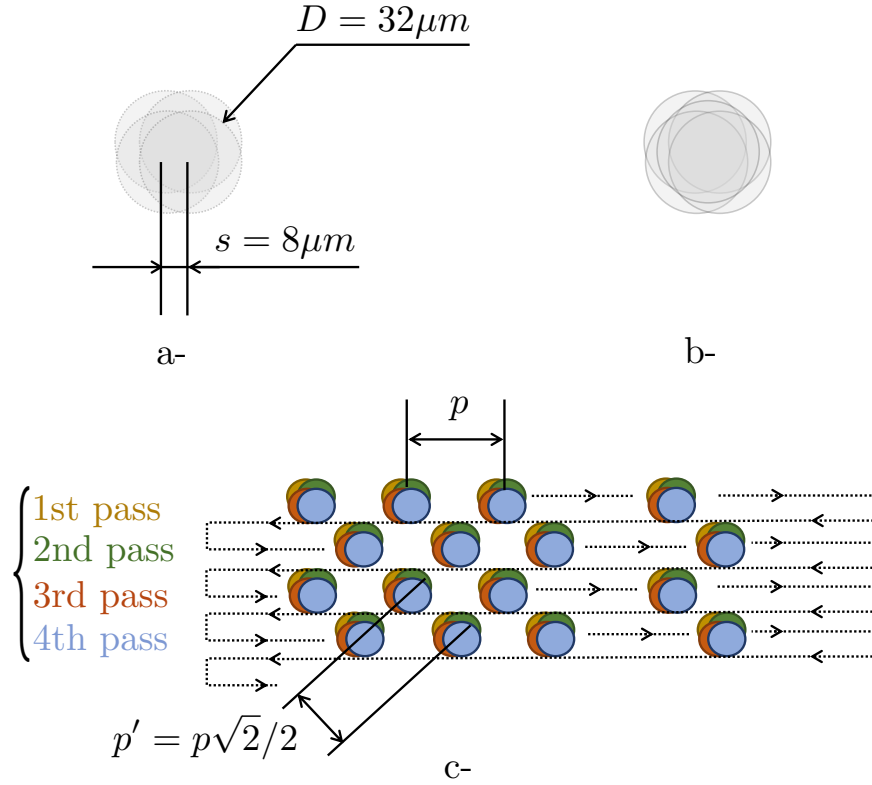


Figure 1: Schematic view illustrating the printing procedure. a- Option 1: printing four shifted dots to approximate a square. b- Option 2: same as a- but with a fifth dot at the center. c- Principle of the checkerboard printing procedure illustrated with Option 1. The checkerboard is printed in different passes, each of them being represented by a different color, thus each set of dots of the same color is printed during the same pass along parallel horizontal lines.

We give here the final values that we obtained for the five parameters corresponding to the best solution. The intermediate results of the trial and error procedure employed to reach this goal are not presented for the sake of brevity and clarity. These five best parameters are gathered in Table 1. Though fixed at its minimum value, a pulse frequency equal to 40 kHz means that 40,000 dots can be

Parameter	Optimal value
Laser power	100%
Spot variable	offset=0
Repetition	20
Scan speed	4,000 mm/s
Pulse frequency	40 kHz

Table 1: Optimal settings for printing a checkerboard of period $p = 100 \mu\text{m}$ with 5 dots of diameter $32 \mu\text{m}$ per “square” and shift $d = 8 \mu\text{m}$. For steel only, 4 dots per “square” give a better contrast than 5 dots

plotted per second. One cm^2 being covered by 10,000 squares, 20 repetitions and 5 dots being used to form each black square, $4 \times 20 \times 5 = 400 \text{ s} = 6\text{mn } 40\text{s}$ were necessary to mark one cm^2 , which is approximately in agreement with what was observed when marking the specimens tested during this study.

2.4. Result on different types of materials

The laser marker was employed on various types of materials, which were all spray painted in white beforehand. Two types of polymers, namely plexiglass and polyethylene, as well as aluminium, steel and wood were considered. Figure 2 shows a closeup view of the patterns obtained on these different materials.

It can be observed that the resulting pattern is well contrasted in each case. Some local defects can be detected, in a sense that some squares expected to be white are actually gray or even black. We will see in the examples below that these defects do not really cause any visible flaws in the displacement and strain maps. The reason is that they are too localized to be detectable by the measuring technique or that the displacement compensation technique recalled in Section 3.3.1 below enables us to get rid of them.

3. Assessing the metrological performance

The objective here is to compare the quality of the displacement and strain maps obtained by using the type of engraved pattern described above instead of the one classically transferred from printed polymeric sheets by using the procedure described in [25]. These two types of checkerboards are respectively referred to as CKB1 and CKB2 in the following.

3.1. Experimental procedure

CKB1 and CKB2 were engraved on the same open-hole parallelepipedic specimen made of aluminum alloy (dimensions: $250 \times 50 \times 1.5 \text{ mm}^2$) in order to facilitate the comparison between the results obtained with each type of checkerboard, see Figure 3. The diameter of the hole was equal to 12 mm. CKB1 was printed on the left-hand side of the specimen while CKB2 was deposited on the right-hand side. Both patterns were about $80 \times 25 \text{ mm}^2$ in size, featured a period p equal of $p = 100 \text{ }\mu\text{m}$. Both were inclined by about 10 degrees with respect to the borders of the images in order to avoid any parasitic fringes in the strain maps due to aliasing, as suggested in [30].

A picture of this specimen is shown in Figure 4. It can be seen in this picture that CKB1 is globally brighter than CKB2. To perform a fair comparison, it was thus necessary to adjust the shutter time in such a way that the best contrast could be obtained for both types of patterns. The aperture of the lens was equal to f/5.6 in both cases in order to stabilize this parameters which influences the PSF affecting the images. Two types of images were captured in turn: one for each type of pattern. As described in [31], the optimal setting was obtained for each type of pattern by *i*– adjusting the focus of the lens, *ii*– plotting the histogram of the gray level distribution and *iii*– choosing the shutter time in such a way that the right-hand tail of the histogram was tangent to the maximum value of the gray level, namely 255. This shutter time was equal to 5.8 ms and 16.5 ms for CKB1 and CKB2, respectively. Indeed, it is demonstrated in [32] that the higher the contrast, the lower the sensor noise propagation to the final displacement and strain maps, so it is important to maximise this contrast for each type of checkerboard to get the lowest possible noise in the final displacement and strain maps. This point will also be discussed later on in this this paper.

The same procedure was applied to process images of CKB1 and CKB2 to extract the corresponding displacement fields, the nominal period being the same for these two patterns. Only the angle between the vertical border of the specimen and the principal axes of symmetry of the checkerboard slightly changed from one case to another. The precise value of this angle was obtained by merely measuring the orientation of the fundamental peaks in the spectrograms of the CKB1 and CKB2 images.

The camera used to capture the images was a Prosilica GT 6600 featuring a CCD sensor of size $6576 \times 4384 \simeq 28.8\text{E}+06$ pixels, with a gray depth equal to 8 bits. The lens was a Nikkor Micro 200 F4 AF-D. Two LED light sources were placed symmetrically along the left- and right-hand sides of the specimen. The specimen was fixed in such a way that its border was aligned with the rows of pixels of the camera. Figure 5 shows the open-hole specimen placed in the experimental setup.

3.2. How to process checkerboard images to extract displacement fields? A brief reminder

The same procedure was employed to extract the displacement and strain fields from the images of CKB1 and CKB2. It is based on the so-called Localized Spectrum Analysis (LSA), which consists in first applying to the images a Windowed Fourier Transform (WFT) with a unique frequency equal to the mean value of the period $p' = p\sqrt{2}/2$ of the checkerboard along the diagonals of its natural axes of symmetry, p being the period along these natural axes, see Figure 1 where these quantities are represented. The phase distribution for both the reference and the deformed images are then calculated by taking the argument of the result of the WFT (the WFT of an image gives a distribution of complex numbers defined at each pixel). The displacement field is finally deduced by using the following expression:

$$\underline{u}(\underline{x}) = -\frac{p}{2\pi} \left(\underline{\Phi}^{cur}(\underline{x} + \underline{u}(\underline{x})) - \underline{\Phi}^{ref}(\underline{x}) \right) \quad (1)$$

where \underline{u} is the sought displacement field, $\underline{\Phi}^{cur}$ and $\underline{\Phi}^{ref}$ contain two phase distributions, namely one along each direction of the reference and current images, respectively. \underline{u} is involved in both parts of this equation. It is retrieved by using the fixed-point algorithm, which rapidly converges here, one iteration being generally sufficient [33]. Directly subtracting the phase maps without performing this compensation of the displacement between current and reference images causes parasitic fluctuation of the frequency of the checkerboard to impair the quality of the strain maps.

The window used in the WFT is a Gaussian envelope. Such a window gives the best tradeoff between various constraints [34]. The function defining this Gaussian window is given by the following equation:

$$w(\underline{x}) = \frac{1}{2\pi\ell^2} e^{\left(-\frac{\|\underline{x}\|^2}{2\ell^2}\right)} \quad (2)$$

where ℓ is the standard deviation and $\|\underline{x}\|$ denotes the norm of vector \underline{x} . This is a handy parameter which can be adjusted by the user to decrease the noise level in the strain maps, as discussed specifically in Section 3.3.2. The price to pay is however that the spatial resolution is impaired in proportion.

All details concerning this measuring technique can be found in Refs [33, 19].

3.3. Results

3.3.1. *Experiment #1: fluctuation of the nominal frequency of the patterns and experimental evidence of the benefit of the displacement compensation*

In Equation 1 above, it can be seen that the current (Φ^{cur}) and reference (Φ^{ref}) phase distributions are subtracted. The displacement is accounted for in the expression of the former to subtract these quantities exactly at the same physical point. Indeed, as illustrated in [35], periodic patterns are potentially corrupted by slight fluctuations of their frequency around their nominal value, and these fluctuations may be erroneously considered as caused by the actual deformation of the surface of the specimen. These fluctuations should therefore be removed and this is precisely what is done by compensating the effect of the displacement in Equation 1, where u_1 and u_2 are taken into account in the expression of Φ^{cur} . The present printing device also has some intrinsic limitations in terms of frequency consistency of the periodic patterns which were engraved. As an example, Figures 6-a and -b show Φ_1 extracted from the image of CKB1 in the reference and current configurations, respectively. These phases were obtained by using the WFT discussed in Section 3.1. No suspicious high-frequency fluctuation can be detected to the naked eye, the phase only gently evolving over the surface of the specimen. Differentiating this quantity with respect to x_1 (by using the `gradient` function of Matlab) enables us to amplify tiny local fluctuations. This is illustrated in Figures 6-c and -d, where $\partial\Phi_1^{cur}/\partial x_1$ is represented. Slight regular “welts” are clearly visible. They are presumably due to the printing device, which cannot print for some technical reason the checkerboard with a rigorously constant period. In particular, it is worth remembering that the distance between two consecutive dots along the horizontal lines in Figure 1 is controlled by the pulse frequency while the distance between two

horizontal lines is given in the dxf file, the controller then imposing this vertical shift. This difference may affect the repeatability of the pattern along the vertical and horizontal directions. Directly subtracting the current and reference phases without any compensation to compute the displacement, thus by using the following equation instead of Equation 1:

$$\tilde{u}(\underline{x}) = -\frac{P}{2\pi} \left(\Phi^{cur}(\underline{x}) - \Phi^{ref}(\underline{x}) \right), \quad (3)$$

where the expression of Φ^{cur} does not take into account \underline{u} (we have $\Phi^{cur}(\underline{x})$ in Equation 3 instead of $\Phi^{cur}(\underline{x} + \underline{u}(\underline{x}))$ in Equation 1), leads to a displacement field denoted by \tilde{u} . This displacement is corrupted by these potential defects. Again, this is not really detectable in the \tilde{u}_1 map (not shown here). Estimating the longitudinal strain $\tilde{\varepsilon}_{11}$ by differentiating \tilde{u}_1 by using the `gradient` function of Matlab shows that this strain distribution is skewed by these defects. This is clearly visible in Figure 6-e. The same pattern as in Figure 6-c and -d can be observed twice, which is due to the fact that these defects affect both Φ^{cur} and Φ^{ref} , and that these quantities are not subtracted at the same physical point. The slight shift in between is caused by the displacement of the physical points between their reference and current positions. On the contrary, resorting to compensation to estimate the displacement (thus using Equation 1 instead of Equation 3), enables us to get rid of these parasitic pattern in the strain maps, as illustrated in Figure 6-f. Note that similar maps (not shown here) are obtained for the other derivatives and strain components.

Figure 7 shows the same quantities as in Figure 6, but for CKB2 instead of CKB1. It can be seen that the defects are less pronounced and more diffuse for CKB2. Again, the benefit of using motion compensation is clearly highlighted when comparing Figure 7-e and Figure 7-f. In Figure 7-f, the slight increase of ε_{11} due to the presence of the hole barely emerges from the noise floor, on the right-hand side of the hole. This phenomenon is less visible in Figure 6-f, probably because the load is not perfectly symmetric.

The reader may wonder whether the compensation is also efficient for greater values of the displacement and strain. Figures 8 and 9 give the response since a higher value for the load is considered

here, namely 3500 N instead of 500 N. It can be seen that the amplitude of the actual strain becomes greater than the parasitic strain due to the fluctuation of the nominal frequency of the checkerboard, but applying the compensation of the displacement still gives a significant improvement of the quality of the strain maps since the spurious fluctuations have disappeared without impairing the spatial resolution. The magnitude of the load being here greater than in the preceding case, the strain increase close to the hole is higher. It is therefore clearly visible in the maps obtained with both patterns, see Figures 8-f and 9-f.

In conclusion, apart from the information irreversibly lost when sampling and quantifying the information in the numerical images, the only sources of error due to image processing which affect the displacement and strain maps are:

1. sensor noise propagation, which causes a random error in the displacement and strain maps,
2. the systematic error due to the fact that regardless to the preceding random error, the displacement returned by LSA is not exactly the actual one, but the actual one *convolved* by the kernel used when applying the windowed Fourier transform [36, 37].

This latter effect manifests itself by an attenuation of the amplitude of the highest spatial frequencies which are necessary to represent the true displacement and strain fields. This attenuation causes image blur to appear in the maps, especially in the strain maps. This effect can however be considered as negligible when the actual displacement and strain fields only gently evolve over the surface of the specimen [38], which is the case here despite the presence of a hole. The pattern-induced bias recently described in [39, 40] is negligible for periodic patterns such as checkerboards [41]. It is also worth remembering that other sources of error such as distortion, non-parallelism between sensor and specimen or parasitic out-of-plane movement may also affect the final results, but they are not discussed in this study.

In the following, we focus our attention on the first of the two effects listed above, which enables us to assess the measurement resolution for the displacement and for the strain (see definition in the Appendix), and for each of the two marking techniques used to prepare the specimen shown in

Figure 3. Other metrological parameters of interest for full-field measurement techniques such as the systematic error due the blur discussed above or the spatial resolution (as defined in [42]) are either negligible or identical for both techniques. They are therefore not considered here. Note that the spatial resolution is the same because the same period p is considered for both CKB1 and CKB2, and the same standard deviation ℓ of the Gaussian envelope in Equation 2 is used when processing with LSA the images obtained with both types of patterns.

3.3.2. Experiment #2: assessment of the displacement and strain resolutions obtained with CKB1 and CKB2

Principle. The objective here is to assess the displacement and strain resolutions obtained with CKB1 and CKB2 by focusing on the propagation of sensor noise to the final displacement and strain maps. We still considered for this the specimen shown in Figure 4. 200 pictures were taken in the reference configuration and 200 others after applying a tensile force equal to 500 N. At each level, half of these 200 images were taken with settings optimized for CKB1 and the other half with settings optimized for CKB2. This stack of images enabled us to calculate, for each of the two patterns, 100 displacement and strain maps, and to deduce the pixelwise distribution of the standard deviation of each displacement and strain component. It is worth remembering that only the shutter time was changed when taking the images of CKB1 and CKB2, the focus and the aperture being unchanged. The equivalent standard deviation for the displacement, defined by

$$\sigma_{equ} = \sqrt{\frac{1}{N} \sum_{k=1}^N std^2(u_j(x_k, y_k))} \quad j = x \text{ or } j = y \quad (4)$$

has also been calculated in each case. This quantity reflects the average noise level in the displacement maps obtained for each patterns. The same quantity is introduced for the strain components. For this quantity and by definition, σ_ε is $\sqrt{2}$ smaller for the shear strain ε_{12} than for the normal strain components ε_{11} and ε_{22} [37]. It is worth emphasizing that performing reliable experiments is somewhat tricky because any tiny movement between camera and specimen may potentially influence the pixelwise estimation of the standard deviation of the displacement along time. As in similar studies

aimed at assessing the metrological performance of full-field measurement techniques, [19] for instance, the average displacement was subtracted for each of the displacement maps to get rid of the influence of micro-translations on the apparent value of σ_{equ} .

Sensor noise propagation has been studied in [36] and theoretical results were verified in [32]. The predictive formulas for the standard deviation of the noise in displacement and strain maps read as follows:

$$\left\{ \begin{array}{ll} \sigma_u &= \left(\frac{p'}{4\ell\pi^{3/2}} \right) \times \left(\frac{1}{K} \right) \times \sigma_{image} \quad \text{for displacement components and} \\ \sigma_\varepsilon &= \left(\frac{p'\sqrt{2}}{8\ell^2\pi^{3/2}} \right) \times \left(\frac{1}{K} \right) \times \sigma_{image} \quad \text{for normal strain components,} \end{array} \right. \quad (5)$$

where:

- σ_u and σ_ε are the standard deviation of the noise in the displacement and strain maps, respectively;
- p' is the period of the periodic pattern along its diagonals. p being the period of the checkerboard along its natural axes of symmetry, p' is equal to $p' = p \times \frac{\sqrt{2}}{2} = 100 \times \frac{\sqrt{2}}{2} \simeq 70.7 \mu\text{m}$ for both CKB1 and CKB2, see Figure 1 where p and p' are represented;
- ℓ is the standard deviation of the Gaussian envelope used as a kernel in the WFT, see Equation 2 above. This quantity is set to $\ell = p = 100 \mu\text{m}$ in the examples shown below;
- σ_{image} is the standard deviation of the noise affecting the images, this noise being assumed to be homoscedastically distributed while noise affecting real image is heteroscedastic [43]. Note that heteroscedastic noise can be stabilized and changed into homoscedastic noise by using the Generalized Anscombe Transform [44] but this procedure has not been applied since we do not use this equation to thoroughly predict the noise level in displacement and strain maps, but to discuss the parameters influencing sensor noise propagation to this maps;
- K is the modulus of the WFT used in LSA. For a periodic function, this modulus is theoretically

equal to [36]:

$$K = \frac{|d_1|\gamma A}{2} \quad (6)$$

where γ is the contrast defined as a coefficient lying between 0 and 1, and A the amplitude of the periodic function. $|d_1|$ is the modulus of the coefficient of the first non-constant term in the Fourier expansion of the function describing the periodic profile. This coefficient reflects the “closeness” of this function to a pure sine function. The higher this coefficient, the better this closeness.

Following these equations, it is clear that the higher the value of γA , the higher the value of K and the lower the value of the noise in the maps. Since we seek the best performance for the measuring system at hand and since we try to highlight the influence of the pattern, it was decided to keep only a region (denoted by \mathcal{D}) of each pattern image for the assessment of the noise in both the displacement and strain maps. \mathcal{D} is defined for each pattern by the region where K is greater than a threshold value equal to 50% of the maximum value of K over the checkerboard image. The border of the zone covered by \mathcal{D} is plotted in blue for each type of pattern in Figure 4.

Results. Figure 10 shows the histograms of the standard deviation of the in-plane displacement components u_1 and u_2 calculated pixelwise from the stack of images. These quantities are calculated only for the pixels within domain \mathcal{D} defined for CKB1 and CKB2.

As in other recent studies using the same type of procedure to quantify the noise in displacement maps [19, 38], the shape of these histograms is not exactly a nice and smooth Gaussian curve, which is probably due to the fact that some tiny parasitic movements are not perfectly eliminated. The noise level is also slightly greater along the loading direction (direction 1), which is consistent with the results obtained in [19] with similar experiments. The main conclusion is however that the noise level is similar for CKB1 and CKB2.

Considering now the strain maps enables us to completely get rid of the effect of in-plane parasitic

movements. The histograms of the distribution of the standard deviation over \mathcal{D} of the three in-plane strain components are represented in Figure 11. These histograms are much smoother than their counterparts plotted in the preceding figure for the displacement components. As expected, the results are similar along directions 1 and 2. The noise level is lower for the shear strain, which is logical since by definition, it is expected to be $\sqrt{2}$ times lower than for the normal strains along directions 1 and 2. A ratio close to $\sqrt{2}$ is obtained with these experimental results: for instance, for ε_{11} , if we multiply by $\sqrt{2}$ the standard deviation obtained for ε_{12} for CKB1, we have $\sigma_{equ} \times \sqrt{2} = 1.71 \times \sqrt{2} \simeq 2.41$ instead of 2.45 which is observed in the experiment. Similar ratios are obtained for ε_{22} as well as for CKB2. Again, the main conclusion is that the noise level is only slightly greater with CKB1 than with CKB2 while the effort and time required to deposit CKB1 is much lower than for CKB2. In addition, no adhesive layer is deposited, only a thin paint layer being sprayed before engraving the pattern. The thickness of the coat of paint has been measured with a measuring column. It is equal to about $20 - 30 \mu\text{m}$, which is much lower than the thickness of the white adhesive, which is generally observed to be equal to some tenths of mm, depending on the skill of the experimentalist. This is certainly much more favorable for studying crack propagation for instance.

The objective of the next section is to illustrate the versatility of the technique by using it in a case for which strain fields are expected to be highly heterogeneous.

3.4. *Experiment #3: measuring the strain field around a knot embedded in a wood specimen*

We considered here a wood specimen of dimensions $250 \times 35 \times 15 \text{ mm}^2$ subjected to a tensile test. A situation for which a knot is embedded in this specimen has been deliberately chosen, see Figure 12-a. Indeed, this knot is expected to behave like an inclusion embedded in an orthotropic material and, as such, to give rise to a heterogeneous strain field around it. In addition, this specimen can be regarded as a stack of early and late wood layers featuring different rigidities. These layers are therefore also expected to give rise to heterogeneous strain distributions with sharp fluctuations. The presence of a crack in the knot (detail A in Figure 12-a) and the wavy aspect of the wood rings (detail B) are also expected to increase the strain heterogeneity in this zone. The objective here was to examine to

what extent such a strain measuring system could be able to reveal fine details in the strain maps. A thin layer of wood filler was applied onto the knot and sanded to obtain the best possible flatness of the specimen in this region. The specimen was then uniformly spray painted in white and the checkerboard was engraved with the laser marker by following the procedure described in Section 2.3. The specimen was finally subjected to a tensile test along direction 1 and images were captured with the same camera as above. The same lighting system as in the preceding experiment was employed. The displacement-controlled loading rate was equal to 1 mm/mn. The shutter time was equal to 5.3 ms and the aperture to f/5.6. The zone marked with the checkerboard is the gray rectangle in Figure 12-b. The natural axes of symmetry of this checkerboard are parallel to the sides of the small squares and aligned with the border of this gray rectangle. It can be seen that this rectangle is slightly inclined with respect to the border of the specimen, as already justified. It can also be observed in Figure 12-b that the gray level is not uniform over the rectangle. Some local fluctuations are visible. They are certainly due to the fact that the paint layer is not perfectly uniform. We will however see that no questionable changes are detected in the strain maps shown below, which is presumably due to the fact that the information is encoded in the phase of the periodic signal, not directly in its amplitude.

We focused our attention on the zone around the knot and thus only plot the strain fields in the region of interest represented by the white dashed box in Figure 12-a. Hence only a small portion of the images is considered here. The three strain fields over this zone are depicted in Figures 13, 14 and 15 for a tensile force equal to $F = 5,000$ N. The local rotation ω_{12} (defined as the antisymmetric part of the displacement gradient) is also given in Figures 16. As in the preceding experiment, these quantities were obtained by setting the standard deviation of the Gaussian used in the WF to $\ell = p$. The calculation time to extract the maps from the deformed and reference images was equal to 3 min and 40 s. The computer used for these calculations was equipped with an 2-core Intel Core i7 5557U @ 3.1Ghz CPU and 16 Gb memory. The following remarks can be drawn from these maps:

- the noise level is quite low compared to value of the actual strain components calculated for this value of the load. The spatial resolution is however sufficiently small to reveal small details in

the strain distribution. The white circle at the bottom right of Figure 13 (see detail D in this figure) has a diameter equal to $6 \times \ell$. This is the apparent width of the Gaussian envelope used to obtain these maps according to the $3 - \sigma$ rule [45], which claims that the apparent diameter of a Gaussian envelope is equal to 6 times its standard deviation. The standard deviation of the Gaussian ℓ being set to $\ell = p$ in this case and the period p of the checkerboard along its natural axes of symmetry being equal to 6.23 pixels=100 μm , it means that the diameter of this circle is equal to 0.6 mm. The calculation of the displacement and strain components being performed pixelwise, it is like these strain maps were obtained with as many strain displacement/strain gages as pixels in these maps, namely about 13 millions in the present case, only a portion of the 28.8 millions of pixels of the camera sensor being used to cover the region of interest. The size of these gages is a circle of diameter 0.6 mm. These gages are shifted between each other by a quantity equal to 1 pixel, thus $100/6.23 \simeq 16 \mu\text{m}$, which means that a significant overlap occurs between these gages. This is the reason why the quantities displayed in these maps are not independent at all the pixels, which can be modeled by a mere convolution of the actual and sought phases of the periodic signal by a kernel which is precisely the Gaussian envelope defined in Equation 2 and used in the WFT [36];

- a striking similarity is observed between the strain maps and the closeup view of the specimen in Figure 12-a. No ground truth is available for this strain distributions, but fine details such as the crack at the middle of the knot (see detail “A” in Figures 12-a) or the wavy wood rings around the knot (see detail “B” in Figures 12-a) are faithfully replicated in the strain maps, especially for ε_{22} and ε_{12} , and for the local rotation map ω_{12} ;
- the shear strain map and the rotation map are more or less antisymmetric with respect to an approximately vertical line passing through the knot;
- increasing the value of the standard deviation ℓ of the Gaussian envelope used in the WFT would directly reduce the noise level in the strain maps. According to Equation 5, multiplying ℓ by

a factor equal to k would reduce (thus improve) the strain resolution by k^2 . The price to pay would be to induce a blur in the fine details given in these maps;

- interestingly, a small piece of dirt is visible at the top left of the three maps. It cannot be removed by using the displacement compensation procedure because it is fixedly connected to the lens and thus does not move with the specimen. The compensation causes a slight shift of this dirt to appear in the maps, which enables us to visually assess the magnitude of the displacement in this zone, see detail “C” in Figure 13.

Conclusion

A procedure for depositing on flat surfaces checkerboard patterns of period as low as $100\text{ }\mu\text{m}$ was discussed in this paper. This technique relies on the use of a laser marker. The main conclusion is that the metrological performance of the measuring system based on this type of marking device is globally the same as the one classically obtained with checkerboards transferred from preprinted sheets with white adhesive. The benefit of using this type of marking device is that checkerboard patterns are obtained in a more systematic way, without any layer of adhesive, and that marking surfaces is much more rapid. It has been shown that the nominal frequency of the checkerboard is not regular, which corrupts the phase derivative maps of the periodic signal which are measured. The final strain maps are however flawless thanks to the displacement compensation used while processing the images.

In some ways, the present study gives a response to a timely issue, namely the definition of the optimal pattern for DIC and the availability of printing means suitable for this pattern. This response is that the optimal pattern for in-plane displacement and strain measurement being checkerboard (because image gradient is maximized) and the latter being periodic, the problem of the minimisation of the optical residual over small regions shall be switched from the spatial domain to the Fourier domain where such a pattern becomes processable. It has been shown in the present paper that such a pattern can be laser marked.

Future studies are necessary to improve the present results:

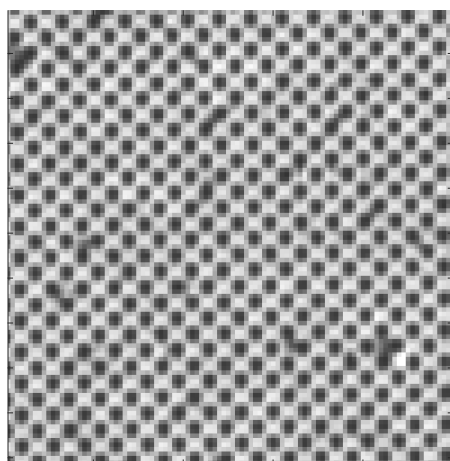
- it would be of interest to see if depositing a coat of paint to increase image contrast, as we did in the present study, could be avoided. Indeed, laser gravers can potentially deposit black and white patterns by adjusting the settings discussed at the beginning of the present paper, but this possibility depends on the nature of the material;
- checkerboards of period equal to $100\text{ }\mu\text{m}$ were engraved in this study, but the technique is perhaps able to print checkerboards with smaller periods. This should be checked with additional printing tests;
- whatever the type of patterning technique, we discussed here a 2D technique, which “only” gives in-plane displacement, strain or rotation components, and not the out-of-plane displacement for instance. A work is currently underway to address this issue in a similar spirit as stereo-DIC.

Acknowledgements

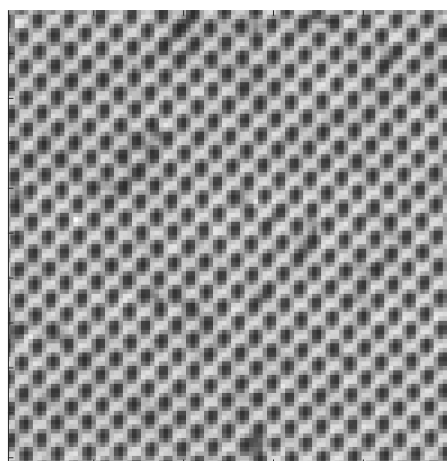
This work has been sponsored by the French government research program “Investissements d’Avenir” through the IDEX-ISITE initiative 16-IDEX-0001 (CAP 20-25). The authors also gratefully acknowledge the financial supports from the French National Research Agency (ANR) through the ICAReS and IMaDe projects (ANR-18-CE08-0028-01 and ANR-19-CE10-0002 grants, respectively), and from the AURA regional council.

Appendix: definition of the measurement resolution

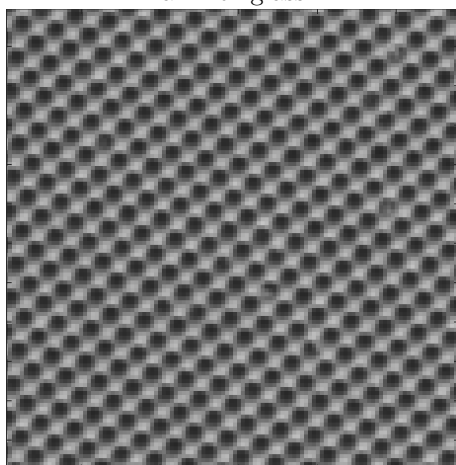
In Ref. [46], the measurement resolution is defined by the *smallest change in a quantity being measured that causes a perceptible change in the corresponding indication*. More precisely, it is proposed in [47] to define it as the *change in quantity being measured that causes a change in the corresponding indication greater than one standard deviation of the measurement noise*, which enables us to quantify the measurement resolution. This definition is quite arbitrary, any other multiple of the standard deviation being also potentially acceptable, but the idea is that the resolution quantifies the smallest change not likely to be caused by measurement noise [47].



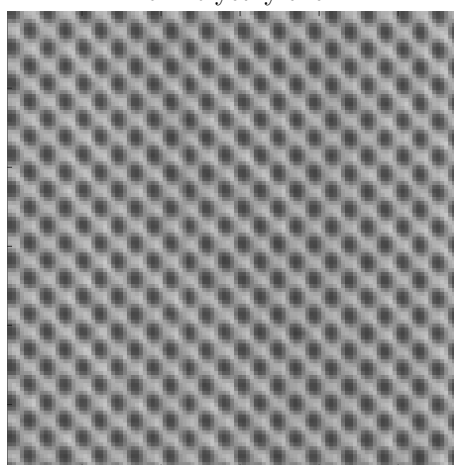
a- Plexiglass



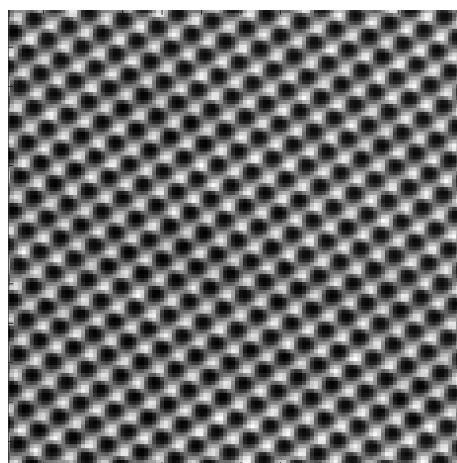
b- Polyethylene



c- Aluminium



d- Steel



e- Wood

Figure 2: Checkerboard obtained by laser marking different materials prepainted in white. Period of the checkerboard along its natural axes of symmetry: $p = 100 \mu\text{m}$

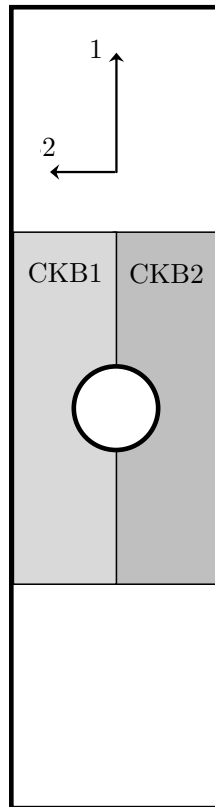


Figure 3: Schematic view of the specimen and location of the two checkerboard patterns CKB1 (engraved) and CKB2 (transferred).

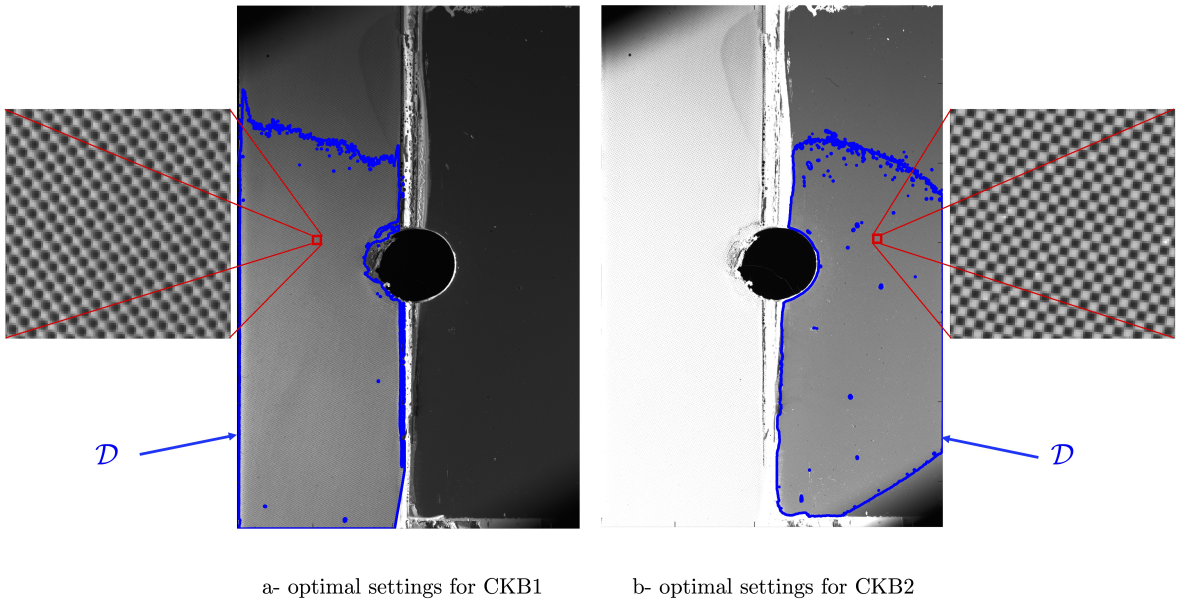


Figure 4: CKB1 and CKB2 as deposited onto the specimen, with lighting optimal for CKB1 (a-) and CKB2 (b-). The border of domain \mathcal{D} used for assessing the noise level in the maps in Section 3.3.2 below is plotted in blue for each pattern.

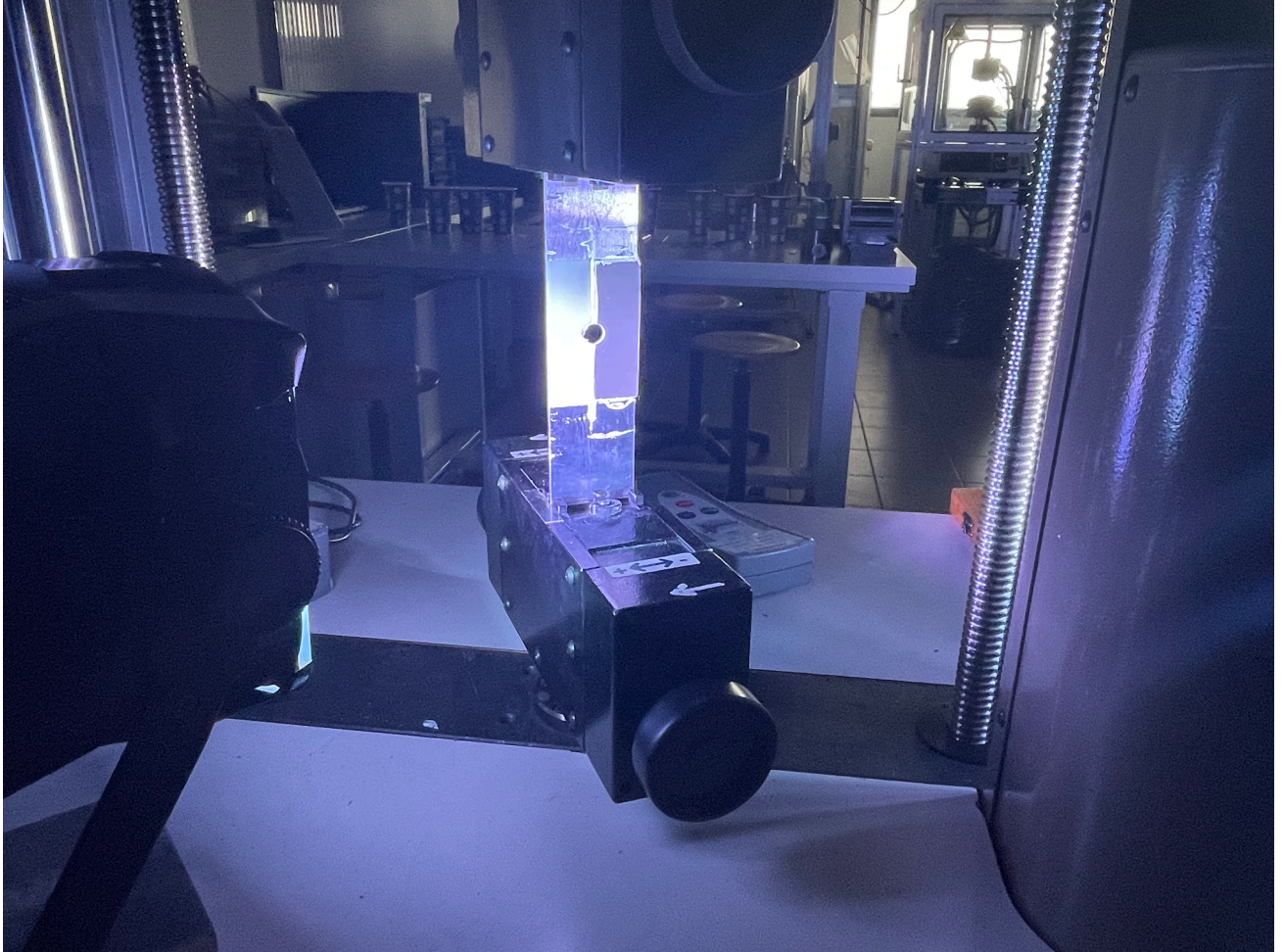


Figure 5: Experimental setup.

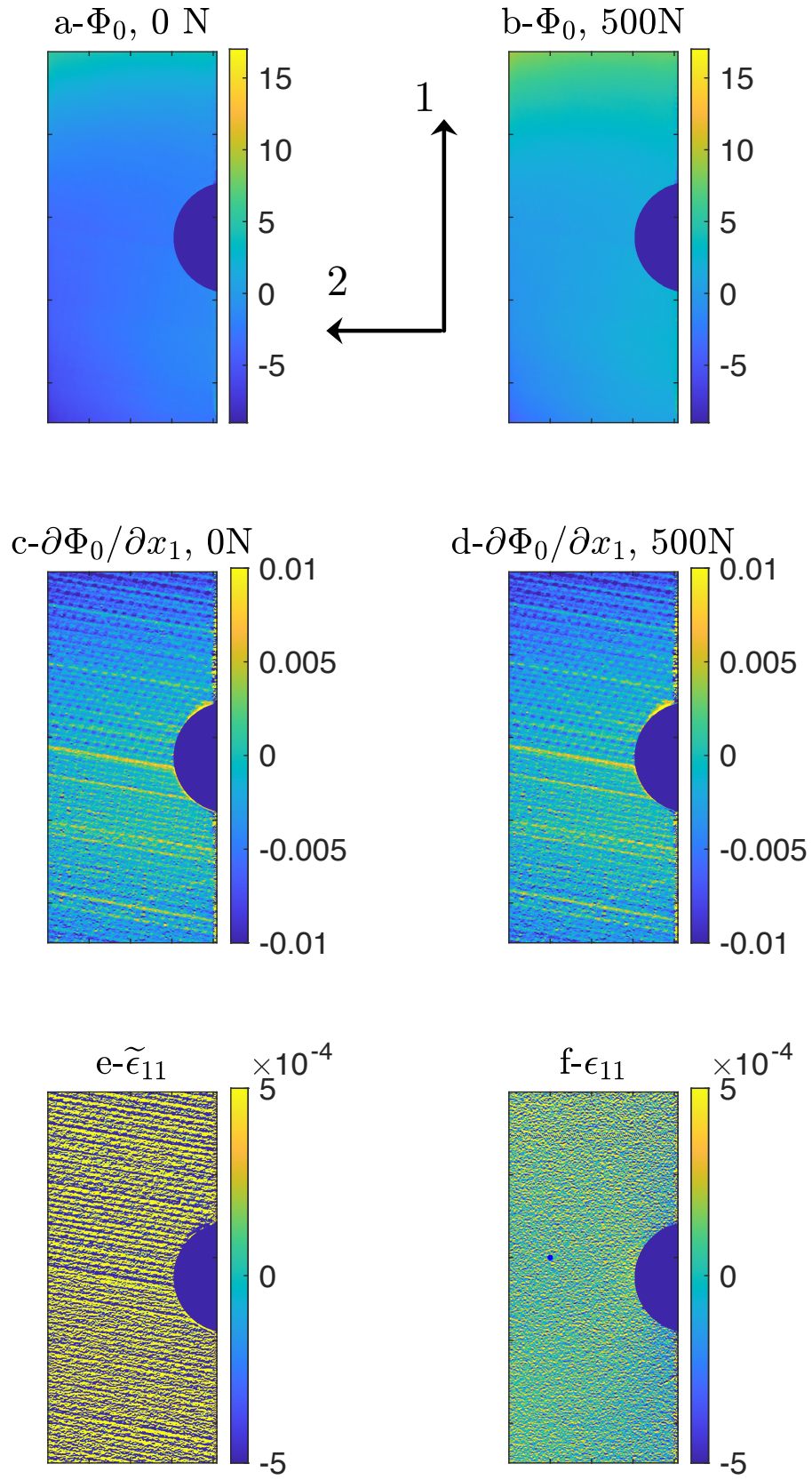


Figure 6: CKB1. a- Φ_1^{ref} at 0 N. b- Φ_1^{cur} at 500 N. c- $\partial\Phi_1^{ref}/\partial x_1$ at 0 N. d- $\partial\Phi_1^{cur}/\partial x_1$ at 500 N. e- $\tilde{\epsilon}_{11}$ calculated with Equation 3. f- ϵ_{11} calculated with Equation 1

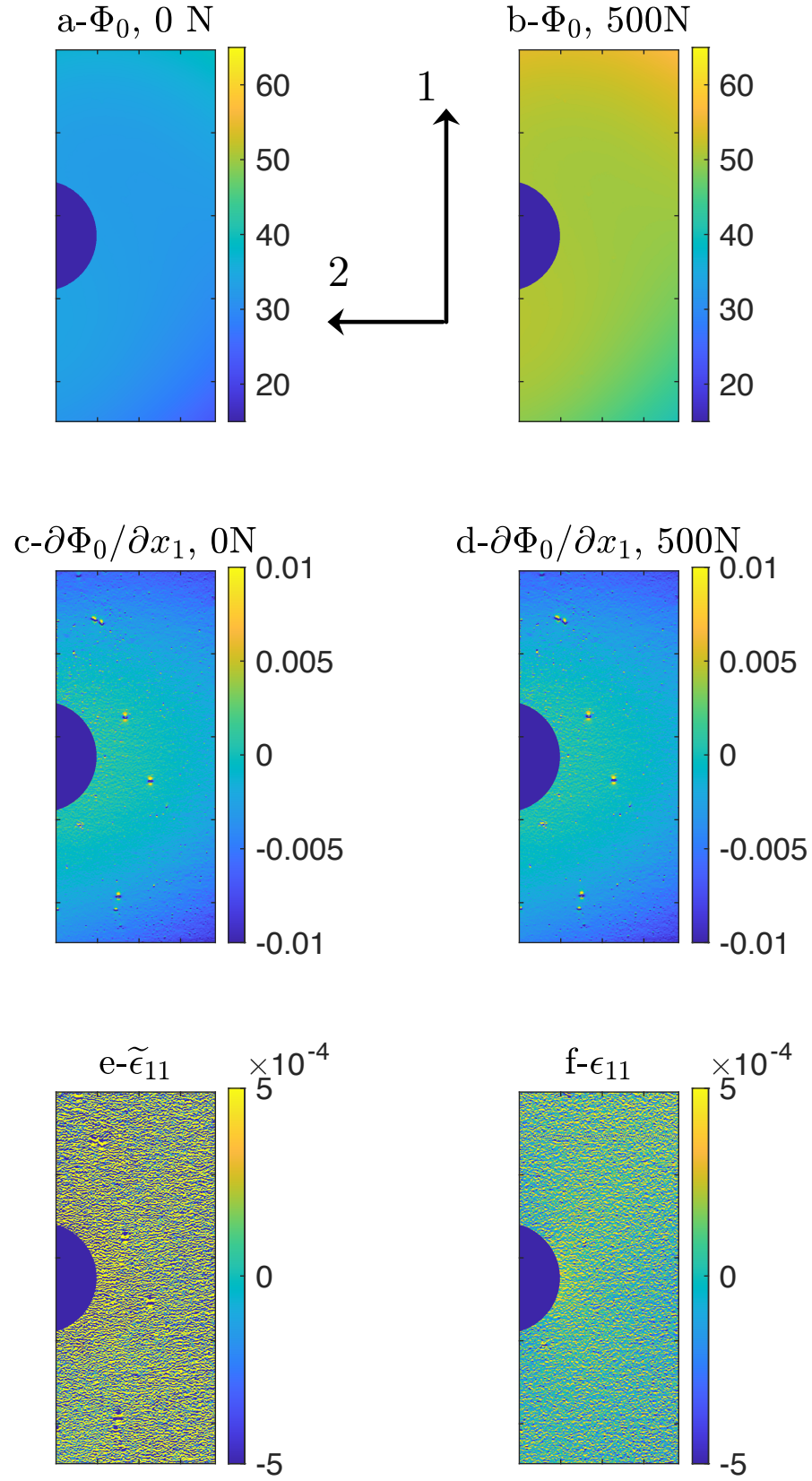


Figure 7: CKB2. a- Φ_1^{ref} at 0 N. b- Φ_1^{cur} at 500 N. c- $\partial\Phi_1^{ref}/\partial x_1$ at 0 N. d- $\partial\Phi_1^{cur}/\partial x_1$ at 500 N. e- $\tilde{\epsilon}_{11}$ calculated with Equation 3. f- ϵ_{11} calculated with Equation 1

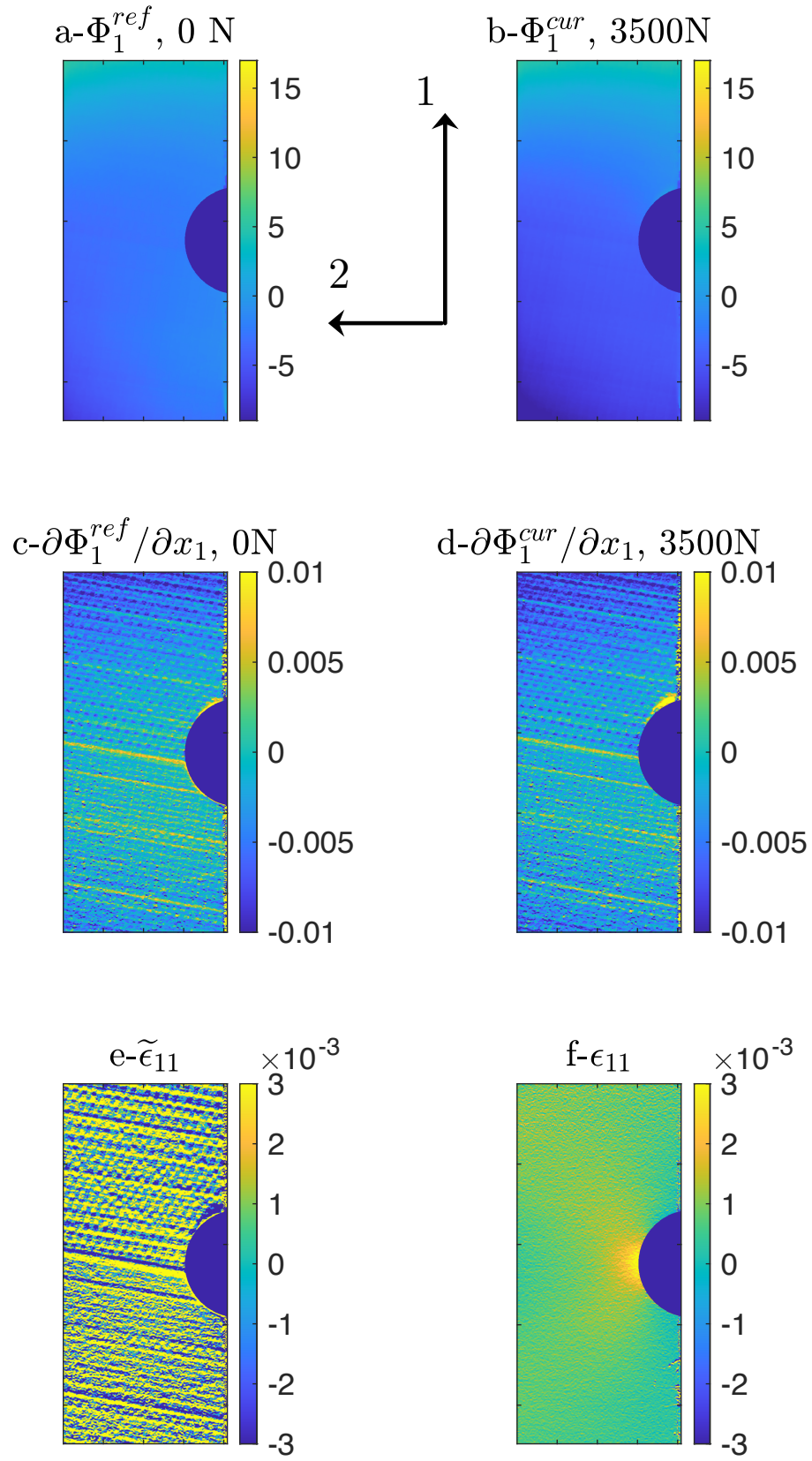


Figure 8: CKB1. a- Φ_1^{ref} at 0 N. b- Φ_1^{cur} at 3500 N. c- $\partial\Phi_1^{ref}/\partial x_1$ at 0 N. d- $\partial\Phi_1^{cur}/\partial x_1$ at 3500 N. e- $\tilde{\epsilon}_{11}$ calculated with Equation 3. f- ϵ_{11} calculated with Equation 1

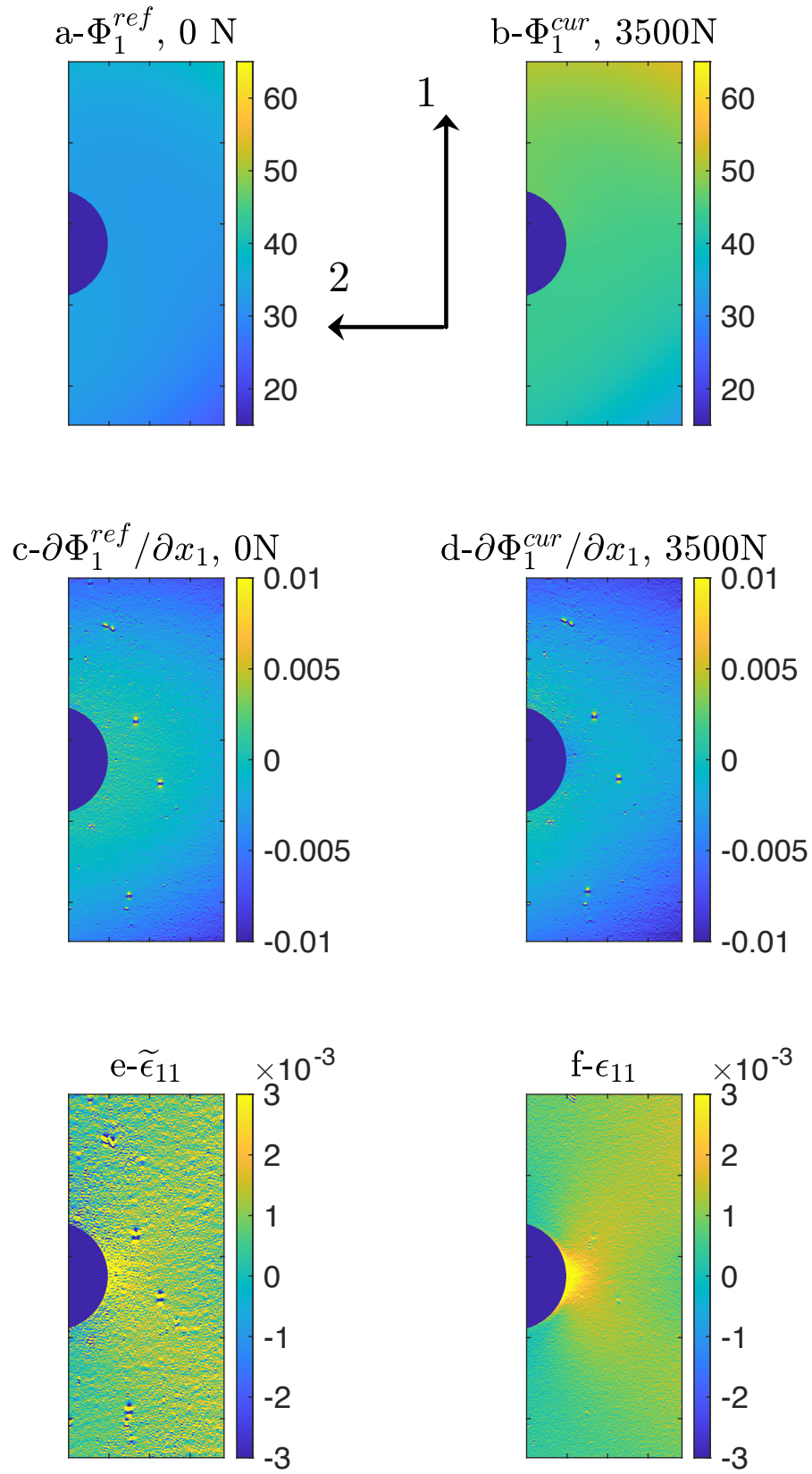
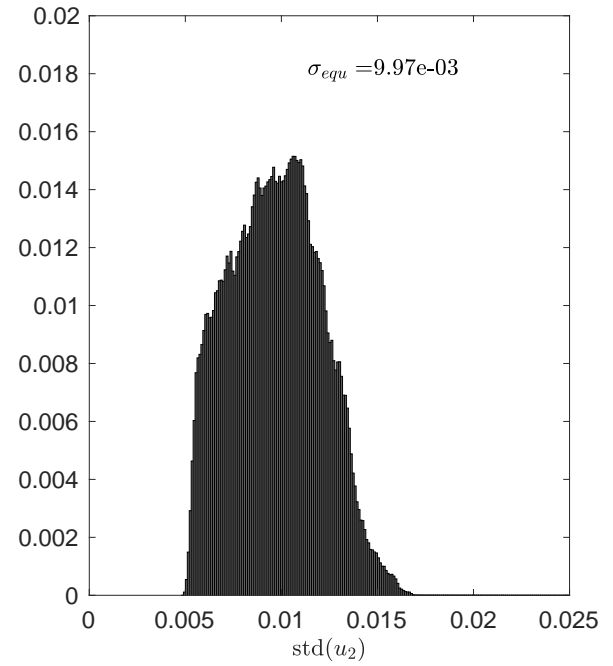
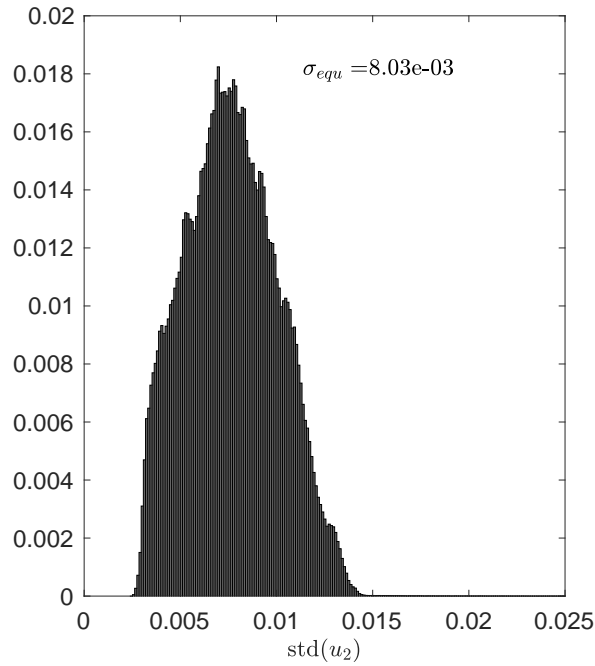
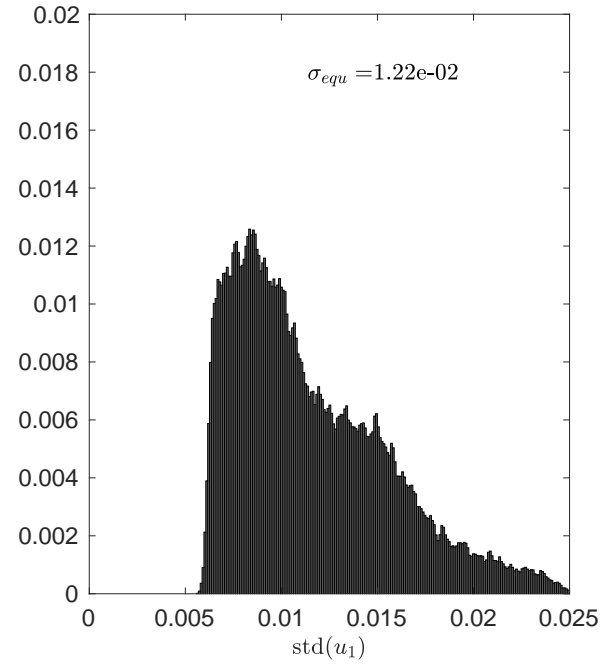
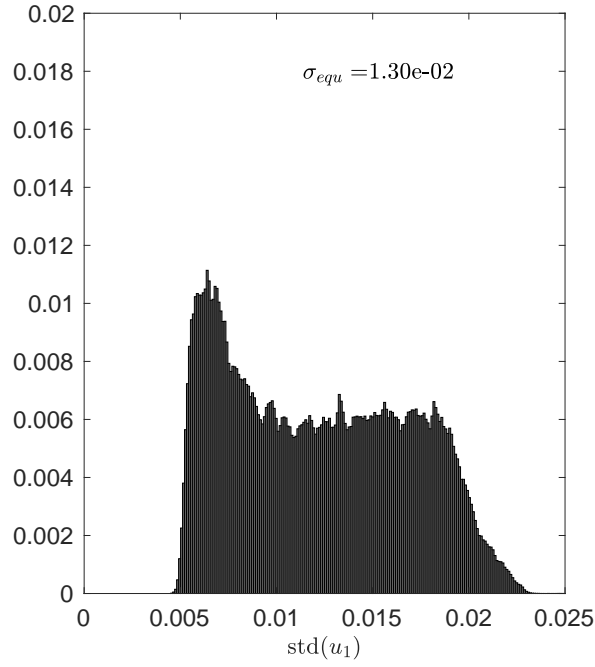


Figure 9: CKB2. a- Φ_1^{ref} at 0 N. b- Φ_1^{cur} at 3500 N. c- $\partial\Phi_1^{ref}/\partial x_1$ at 0 N. d- $\partial\Phi_1^{cur}/\partial x_1$ at 3500 N. e- $\tilde{\epsilon}_{11}$ calculated with Equation 3. f- ϵ_{11} calculated with Equation 1



a- CKB1

b- CKB2

Figure 10: Distribution over \mathcal{D} of the standard deviation for the two in-plane displacement components. a- CKB1. b- CKB2.

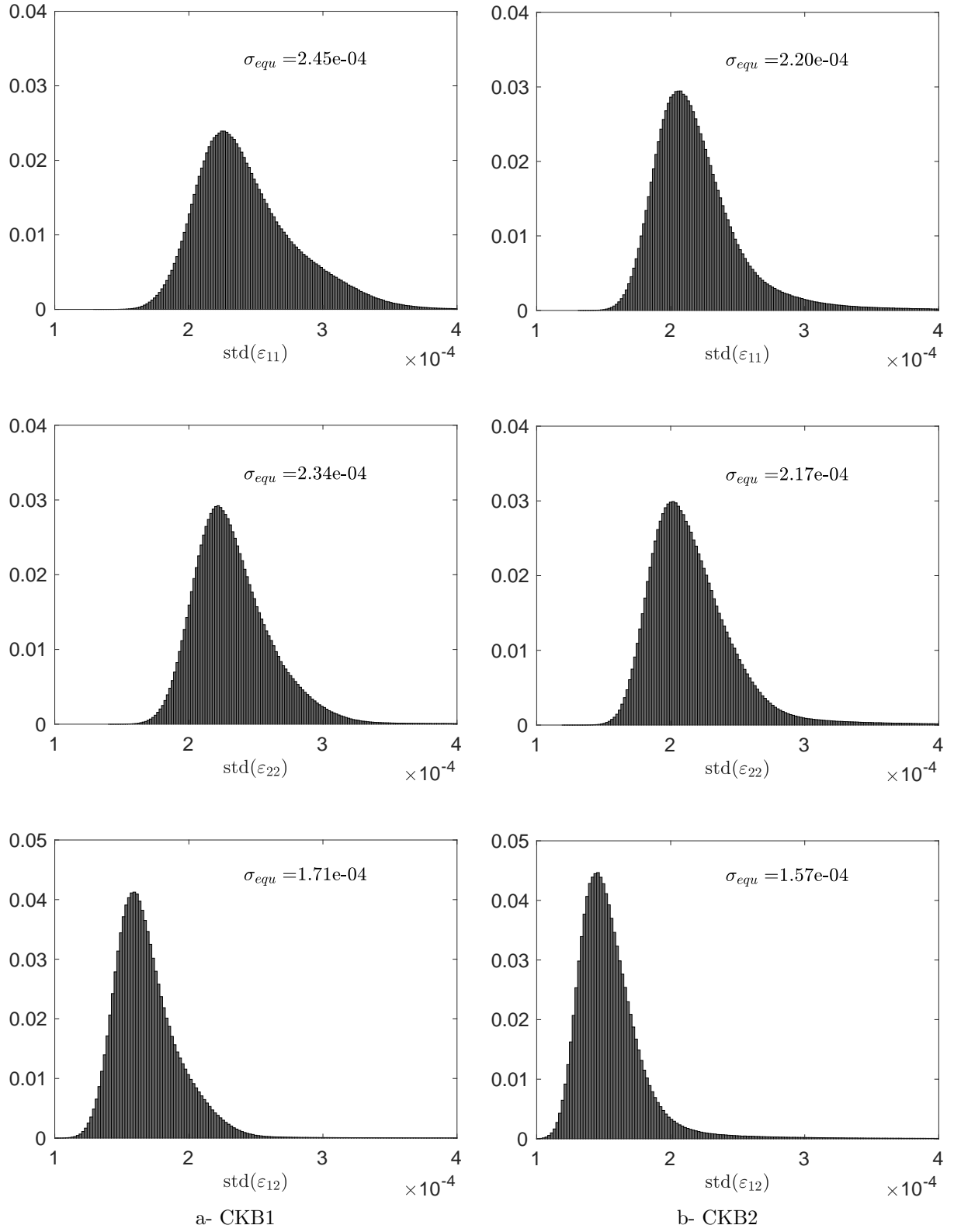
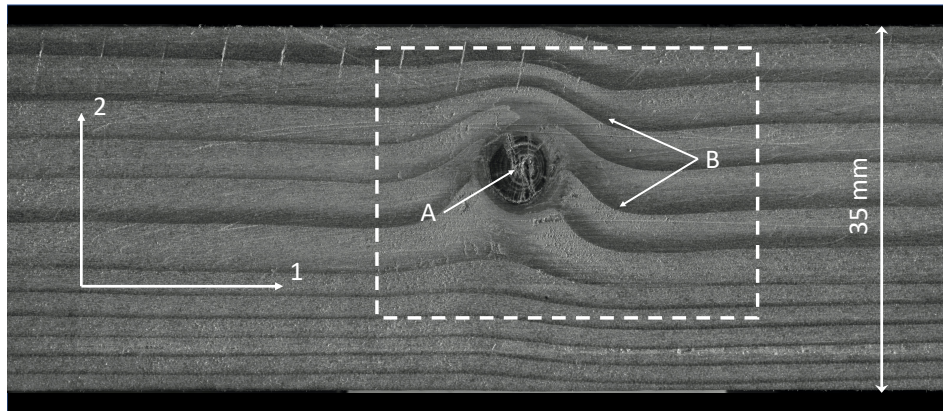


Figure 11: Distribution over \mathcal{D} of the standard deviation for the three in-plane strain components. a- CKB1. b- CKB2.



a- Central zone of the wood specimen and approximate location of the region of interest where strain and local rotation maps are plotted.

A: crack along the diameter of the knot.

B: wavy aspect of the annual rings around the knot.



b- Same zone as in a- after spray painting the specimen in white and engraving the checkerboard pattern by laser marking.

Figure 12: Wood specimen before and after spray painting the surface in white and engraving the checkerboard pattern.

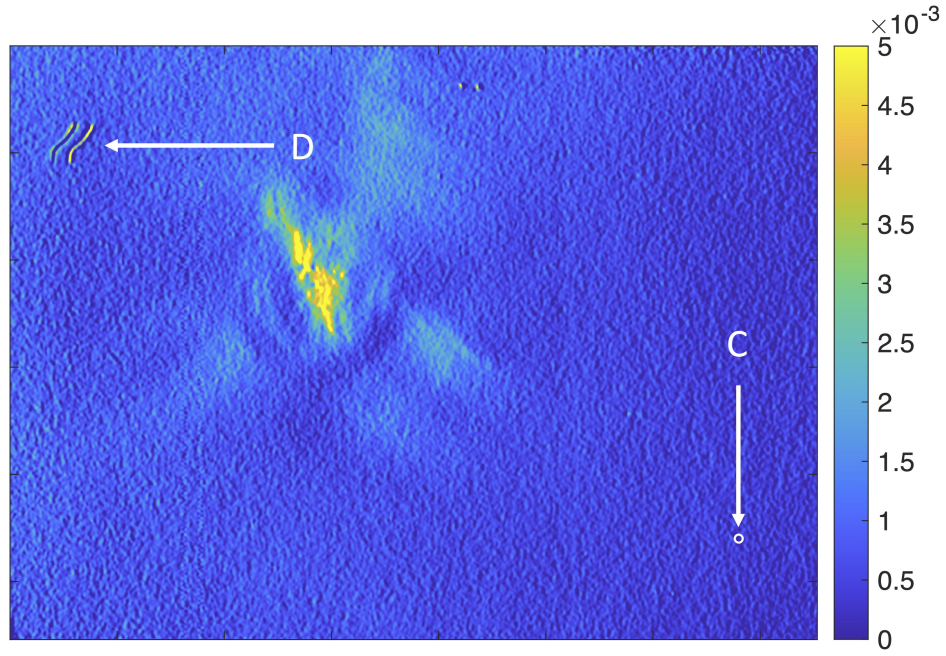


Figure 13: ε_{xx} strain map over the zone of interest shown in Figure 12. C: piece of dust on the sensor giving an idea of the amplitude of the actual displacement between current and reference configurations. D: top view of the Gaussian envelope according to the $3 - \sigma$ rule [45].

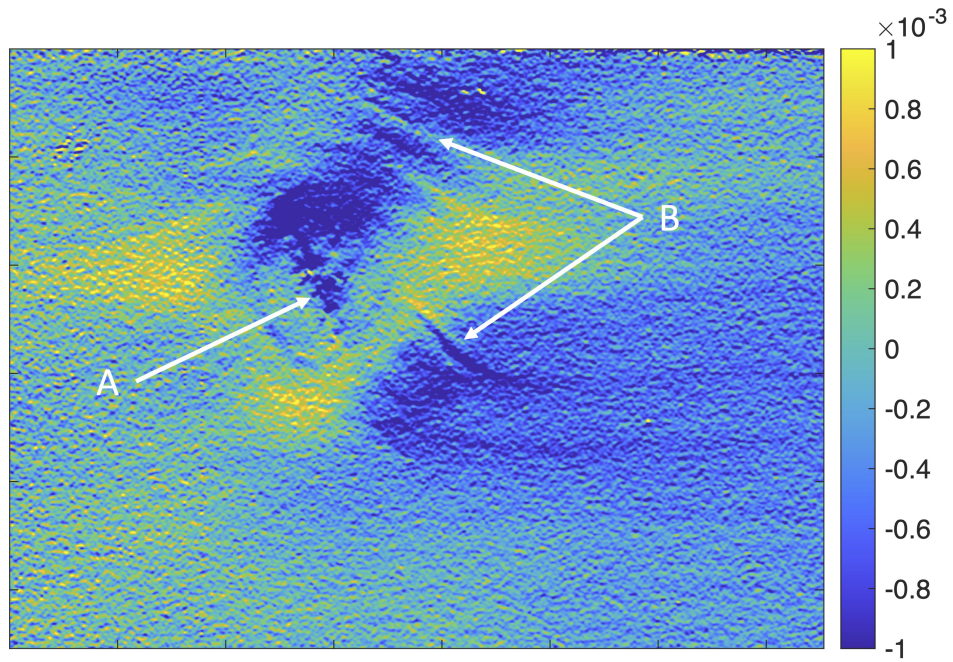


Figure 14: ε_{yy} strain map over the zone of interest shown in Figure 12. See in Figure 12 the crack along the diameter (detail A) and the wavy aspect of the annual rings (detail B).

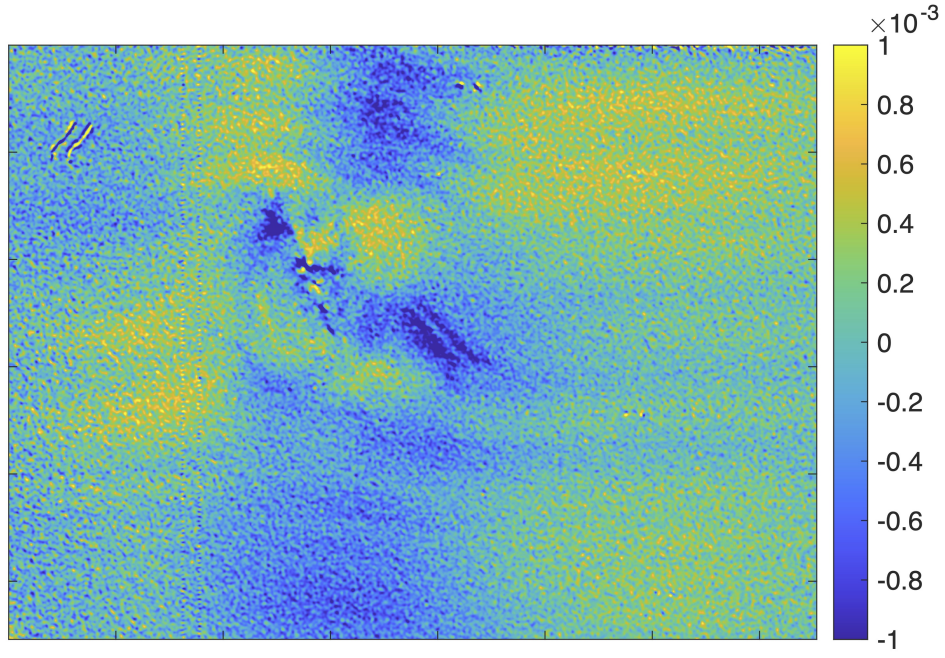


Figure 15: ε_{xy} strain map over the zone of interest shown in Figure 12.

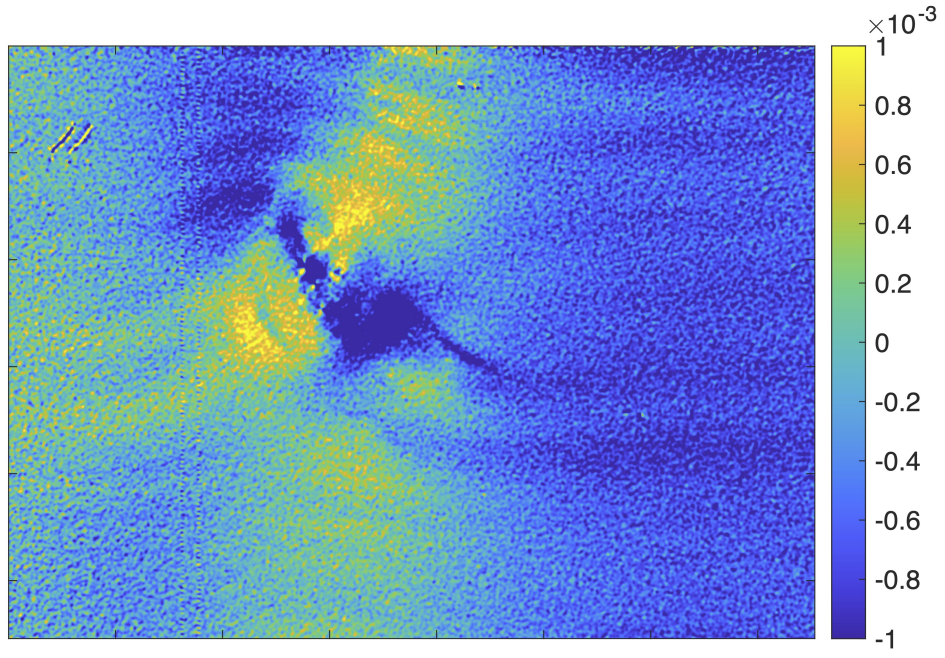


Figure 16: ω_{xy} local rotation map over the zone of interest shown in Figure 12.

References

- [1] F. Pierron and M. Grédiac. Towards material testing 2.0. a review of test design for identification of constitutive parameters from full-field measurements. *Strain*, 57(1):e12370, 2021.
- [2] S. Bossuyt. Optimized patterns for digital image correlation. In *Conference Proceedings of the Society for Experimental Mechanics Series*, volume 3, pages 239–248, 2013.
- [3] G. F. Bomarito, J. D. Hochhalter, T. J. Rugglesb, and A. H. Cannon. Increasing accuracy and precision of digital image correlation through pattern optimization. *Optics and Lasers in Engineering*, 91(April):73–85, 2017.
- [4] G. F. Bomarito, J. D. Hochhalter, T. J. Ruggles, and A. H. Cannon. Increasing accuracy and precision of digital image correlation through pattern optimization. *Optics and Lasers in Engineering*, 91(May 2016):73–85, 2017.
- [5] Y. Su, Q. Zhang, and Z. Gao. Statistical model for speckle pattern optimization. *Opt. Express*, 25(24):30259–30275, Nov 2017.
- [6] A. Lavatelli, R. Balcaen, E. Zappa, and D. Debruyne. Closed-loop optimization of DIC speckle patterns based on simulated experiments. *IEEE Transactions on Instrumentation and Measurement*, 68(11):4376–4386, 2019.
- [7] M. Mathew, B. Wisner, S. Ridwan, M. McCarthy, I. Bartoli, and A. Kontsos. A Bio-Inspired Frequency-Based Approach for Tailorable and Scalable Speckle Pattern Generation. *Experimental Mechanics*, 60(8):1103–1117, 2020.
- [8] R. Fouque, R. Bouclier, J.C. Passieux, and J.N. Périé. Fractal pattern for multiscale digital image correlation. *Experimental Mechanics*, 61(3):483–497, 2021.
- [9] C. C. K. Chan, D. Kumar, and C-H. Chiang. Coarse and fine localized CNN classifier for intelligent DIC preprocessing in large structure health monitoring sample. In Tzu-Yang Yu and

- Andrew L. Gyekenyesi, editors, *Nondestructive Characterization and Monitoring of Advanced Materials, Aerospace, Civil Infrastructure, and Transportation XV*, volume 11592, pages 141 – 152. International Society for Optics and Photonics, SPIE, 2021.
- [10] Y. Wang, Y. Gao, Y. Liu, Z. Gao, Y. Su, and Q. Zhang. Optimal aperture and digital speckle optimization in digital image correlation. *Experimental Mechanics*, 61(4):677–684, 2021.
 - [11] Y. L. Dong and B. Pan. A review of speckle pattern fabrication and assessment for digital image correlation. *Experimental Mechanics*, 57(8):1161–1181, 2017.
 - [12] A. H. Cannon, J. D. Hochhalter, A. W. Mello, G. F. Bomarito, and M. D. Sangid. Microstamping for improved speckle patterns to enable digital image correlation. *Microscopy and Microanalysis*, 21(S3):451–452, 2015.
 - [13] N. Li N, S. Guo, and M.A. Sutton. Recent progress in e-beam lithography for SEM patterning. In *MEMS and Nanotechnology*, volume 2, 2011. Springer, New York.
 - [14] W. A. Scrivens, Y. Luo, M. A. Sutton, S. A. Collette, M. L. Myrick, P. Miney, P. E. Colavita, A. P. Reynolds, and X. Li. Development of patterns for digital image correlation measurements at reduced length scales. *Experimental Mechanics*, 47(1):63–77, 2007.
 - [15] D. M. Hisley, J. C. Gurganus, and A. W. Drysdale. Experimental methodology using digital image correlation to assess ballistic helmet blunt trauma. *Journal of Applied Mechanics*, 78(5), 08 2011.
 - [16] N. Biery, M. de Graef, and T. M. Pollock. A method for measuring microstructural-scale strains using a scanning electron microscope: Applications to γ -titanium aluminides. *Metallurgical and Materials Transactions A*, 34(10):2301–2313, 2003.
 - [17] A. Vinel, R. Seghir, J. Berthe, G. Portemont, and J. Réthoré. Metrological assessment of multi-sensor camera technology for spatially-resolved ultra-high-speed imaging of transient high strain-rate deformation processes. *Strain*, 57(4):e12381, 2021.

- [18] B. Pan, Z. Lu, and H. Xie. Mean intensity gradient: An effective global parameter for quality assessment of the speckle patterns used in digital image correlation. *Optics and Lasers in Engineering*, 48(4):469–477, 2010.
- [19] M. Grédiac, B. Blaysat, and F. Sur. Extracting displacement and strain fields from checkerboard images with the localized spectrum analysis. *Experimental Mechanics*, 59(2):207–218, 2019.
- [20] M. Grédiac, F. Sur, and B. Blaysat. Comparing several spectral methods used to extract displacement and strain fields from checkerboard images. *Optics and Lasers in Engineering*, 127:105984, 2020.
- [21] M. Grédiac, B. Blaysat, and F. Sur. A critical comparison of some metrological parameters characterizing local digital image correlation and grid method. *Experimental Mechanics*, 57(3):871–903, 2017.
- [22] R. Moulart, R. Rotinat, F. Pierron, and G. Lerondel. On the realization of microscopic grids for local strain measurement by direct interferometric photolithography. *Optics and Lasers in Engineering*, 45(12):1131–1147, 2007.
- [23] R. Moulart, R. Rotinat, and F. Pierron. Full-field evaluation of the onset of microplasticity in a steel specimen. *Mechanics of Materials*, 41(11):1207–1222, 2009.
- [24] H. Mirmohammad and O.T. Kingstedt. Theoretical considerations for transitioning the grid method technique to the microscale. *Experimental Mechanics*, 61(5):753–770, 2021.
- [25] J.L. Piro and M. Grédiac. Producing and transferring low-spatial-frequency grids for measuring displacement fields with moiré and grid methods. *Experimental Techniques*, 28(4):23–26, 2004.
- [26] Y. Surrel. Printing grids at the University of Southampton Print Centre. http://photodyn.org/wp-content/uploads/2016/03/Report_UniversityPrintCentre.pdf, 2017. Internal report, University of Southampton.

- [27] Y. Surrel. Printing grids at the University of Southampton Print Centre - Using the ‘High Quality’ mode. http://photodyn.org/wp-content/uploads/2016/03/Report_UniversityPrintCentre_2.pdf, 2017. Internal report, University of Southampton.
- [28] L. Fletcher and J. Van Blitterswyk and F. Pierron. A manual for conducting Image-Based Inertial Impact (IBII) tests. <https://doi.org/10.32720/idics/gpg.ed1>, 2019. Internal report, University of Southampton. DOI: 10.5258/SOTON/P0015.
- [29] Keyence. 3-axis UV laser marker MD-U series. Technical note, 2017.
- [30] F. Sur, B. Blaysat, and M. Grédiac. Determining displacement and strain maps immune from aliasing effect with the grid method. *Optics and Lasers in Engineering*, 86:317–328, 2016.
- [31] S. Qin, M. Grédiac, B. Blaysat, S. Ma, and F. Sur. Influence of the sampling density on the noise level in displacement and strain maps obtained by processing periodic patterns. *Measurement*, 173:108570, 2021.
- [32] M. Grédiac and F. Sur. Effect of sensor noise on the resolution and spatial resolution of the displacement and strain maps obtained with the grid method. *Strain*, 50(1):1–27, 2014. Paper invited for the 50th anniversary of the journal. Wiley.
- [33] M. Grédiac, F. Sur, and B. Blaysat. The grid method for in-plane displacement and strain measurement: a review and analysis. *Strain*, 52(3):205–243, 2016.
- [34] F. Sur and M. Grédiac. Influence of the analysis window on the metrological performance of the grid method. *Journal of Mathematical Imaging and Vision*, 56(3):472–498, 2016.
- [35] C. Badulescu, M. Grédiac, and J.-D. Mathias. Investigation of the grid method for accurate in-plane strain measurement. *Measurement Science and Technology*, 20(9):20:095102, 2009.
- [36] F. Sur and M. Grédiac. Towards deconvolution to enhance the grid method for in-plane strain measurement. *Inverse Problems and Imaging*, 8(1):259–291, 2014. American Institute of Mathematical Sciences.

- [37] M. Grédiac and F. Sur. Effect of sensor noise on the resolution and spatial resolution of the displacement and strain maps obtained with the grid method. *Strain*, 50(1):1–27, 2014. Paper invited for the 50th anniversary of the journal. Wiley.
- [38] M. Grédiac, B. Blaysat, and F. Sur. On the Optimal Pattern for Displacement Field Measurement: Random Speckle and DIC, or Checkerboard and LSA? *Experimental Mechanics*, 60(4):509–534, 2020.
- [39] S.S. Fayad, D.T., Seidl, and P.L. Reu. Spatial DIC errors due to Pattern-Induced Bias and grey level discretization. *Experimental Mechanics*, 60(2):249–263, 2020.
- [40] R.B. Lehoucq, P. L. Reu, and D.Z. Turner. The effect of the ill-posed problem on quantitative error assessment in digital image correlation. *Experimental Mechanics*, 61(3):609–621, 2021.
- [41] F. Sur, B. Blaysat, and M. Grédiac. On biases in displacement estimation for image registration, with a focus on photomechanics. *Journal of Mathematical Imaging and Vision*, 63:777–806, 2021.
- [42] L. Wittevrongel, P. Lava, S. V. Lomov, and D. Debruyne. A self adaptive global digital image correlation algorithm. *Experimental Mechanics*, 55(2):361–378, 2015.
- [43] H. Faraji and W.J. MacLean. CCD noise removal in digital images. *IEEE Transactions on Image Processing*, 15(9):2676–2685, 2006.
- [44] F.J. Anscombe. The transformation of Poisson binomial and negative-binomial data. *Biometrika*, 35(3-4):246–254, 1948.
- [45] E. W. Grafarend. *Linear and Nonlinear Models: Fixed Effects, Random Effects, and Mixed Models*. Walter de Gruyter, 2006.
- [46] International vocabulary of metrology. Basic and general concepts and associated terms, 2008. Third edition.

- [47] A. Chrysochoos and Y. Sirel. Chapter 1. Basics of metrology and introduction to techniques. In M. Grédiac and F. Hild, editors, *Full-field measurements and identification in solid mechanics*, pages 1–29. Wiley, 2012.